

Saturation of electron cyclotron maser by lower-hybrid waves

G. Fleishman¹ and K. Arzner²

¹ Ioffe Institute for Physics and Technology, 194021 St. Petersburg, Russia (gregory@sun.ioffe.rssi.ru)

² Institut für Extraterrestrische Physik, P.O. Box 1603, 85740 Garching, Germany (kja@mpe.mpg.de)

Received 22 July 1999 / Accepted 2 March 2000

Abstract. We perform a numerical study on the quasilinear relaxation of an electron cyclotron maser on the initially dominant mode. We focus thereby on a situation where the initially dominant modes are quasi-electrostatic lower hybrid (lh) waves, which have not been treated in preceding studies. To this end, we chose $0.2 \leq \omega_p/\omega_{Be} < 0.5$ (ω_p : plasma-, ω_{Be} : electron cyclotron frequency) and an initial losscone distribution of energetic electrons of the form $f(p, \mu) \sim p^{-\xi} e^{-\mu^2/\mu_0^2}$ (p : momentum, μ : pitch angle cosine). Superimposed on this is a damping Maxwellian background. From our calculations, we find that multiple peaks in the lower-hybrid wave intensity can occur if the initial loss cone distribution is sufficiently broad. We also find that quasilinear relaxation with respect to lower-hybrid waves does not destroy the capability of the electron distribution to amplify transverse (XOZ) waves, which therefore become dominant at a later stage. The comparison with observations shows that the calculated shape of a single peak in the lower-hybrid energy density displays a remarkable similarity to solar radio spikes.

Key words: Sun: radio radiation – masers

1. Introduction

Radio emission of various cosmic objects is frequently produced by coherent mechanisms (Melrose, 1980). Such radiation is observed from planets (Wu 1985, Ladreiter & Leblanc 1990, Galopeau et al. 1989, Winglee et al. 1992), stars (Bastian et al. 1990) and the sun. Electron cyclotron maser (ECM) emission is one of the coherent mechanisms which is probably responsible for many kinds of the observed radio emission, i.e. for solar millisecond spikes (e.g. Aschwanden 1990a).

In some cases (e.g., for Earth's auroral kilometric radiation), the ECM operation was proved directly by in situ measurements (Wu 1985). Sometimes there is indirect evidence for the ECM operation, but sometimes the type of coherent mechanism is questionable. Generally, it is difficult to distinguish between different coherent mechanisms in observations. A reliable discrimination can only be done based on a detailed comparison of the observations with a well-developed theory. Therefore, it is

very important to further develop the ECM theory, in particular numerically and beyond the limitations of the linear stage.

In a recent review, Fleishman & Melnikov (1998) investigated solar radio spikes and concluded, based on existing theory, that these are produced by ECM emission. Solar radio spikes are observed over a large frequency range (Slotje 1981, Stähli & Magun 1986, Güdel & Benz 1990, Karlicky et al. 1996, Fu & Huang 1998) and known as the shortest and most narrow-band solar bursts. The last two properties clearly suggest coherent emission. As outlined in Fleishman & Melnikov (1998), we concentrate on electron cyclotron masers (ECM) driven by nonthermal electrons with a broad energy spectrum. This mechanism can account for many of the observed features and we consider it as the most likely explanation for solar millisecond spikes.

Whereas the linear growth of an ECM has been extensively studied (Sharma & Vlahos 1984, Melrose et al. 1984, Winglee & Dulk 1986, Li 1986, Aschwanden & Benz 1988, Fleishman & Yastrebov 1994b+ 1994c, Ledenev 1998), its nonlinear saturation was considered in relatively few papers only. Wu et al. 1981 found an analytical solution of the quasilinear equations for an anisotropic Maxwellian distribution of fast electrons after some approximations and simplifications. Pritchett 1986 modified this solution for the DGH distribution (Dory et al. 1965) of fast electrons. The most detailed numerical study of the quasilinear relaxation was performed by Aschwanden 1990b who calculated the evolution of transverse modes of an initially unstable sin-N Maxwellian distribution of fast electrons. Based on these papers and some qualitative estimates derived from the linear growth rate it became commonly accepted that ECM is featured by the following properties:

1. Saturation of the instability occurs for the fastest growing mode and provides a single peak in the wave spectral energy density.
2. The angular distribution of fast particles becomes more or less isotropic.
3. Practically all free energy of fast electrons goes into the amplification of the dominant mode so that other modes are not substantially amplified.
4. The typical saturation time is of order of $(10-15)\Gamma_{max}^{-1}$ with Γ_{max} the maximum growth rate (Aschwanden 1990b found $50\Gamma_{max}^{-1}$).

Send offprint requests to: K. Arzner

The present paper deals with an anisotropic population of fast electrons with a power-law momentum spectrum. Such a broad spectrum fits observations better than the quasi-Maxwellian spectra considered by previous authors (Fleishman & Melnikov 1998). In order to investigate the evolution of a powerlaw-driven ECM, we performed a numerical integration of the quasilinear equations given below. From our calculations, we find that all points mentioned above are not necessarily true for non-electromagnetic waves and non-Maxwellian electron distributions.

2. Definition of the model

According to different parameter regimes and initial distributions of fast electrons, several wave modes can be amplified. Aschwanden (1990b) already discussed the instability driven by an anisotropic (sin-N) Maxwellian distribution of fast electrons. He thereby considered transverse (O/X) modes only. Complementary to Aschwandens study, we concentrate on a situation where certain plasma waves – i.e. lower hybrid waves – have the largest initial growth rate. Such a situation arises if the plasma-to-gyrofrequency ratio $Y \doteq \omega_{pe}/\omega_{Be}$ is from ~ 0.3 to ~ 0.5 and the initial distribution of energetic electrons (per $d^3\mathbf{p} = 2\pi p^2 dp d\mu$) has the form (Fleishman 1994b)

$$f_0(p, \mu) \propto \begin{cases} \left(\frac{p_0}{p}\right)^\xi e^{-\mu^2/\mu_0^2} & p \geq p_0 \\ 1 & 0 \leq p < p_0 \end{cases} \quad (1)$$

with normalization according to

$$2\pi \int_{p_0}^{\infty} p^2 dp \int_{-1}^1 d\mu f_0(p, \mu) = n_b$$

Here, p is the electron momentum per unit mass, μ is the electron pitch angle cosine and n_b is the number density (cm^{-3}) of the energetic electrons which effectively participate in the maser process (for electrons with momentum $p \leq p_0$, the distribution is flat so that these electrons do not affect the growth- or damping rates.) The pitch-angle distribution (1) describes a broad, two-sided loss cone with aperture angle $\arccos \mu_0$ ($\sim \pm 70^\circ$ in our simulations). In addition to the initial energetic component described by Eq. (1), our models has a cold (nonrelativistic) Maxwellian background

$$f_T = n_0 \left(\frac{m}{2\pi kT}\right)^{3/2} e^{-p^2 m/2kT} \quad (2)$$

with $kT \ll mp_0^2$ and $n_0 \gg n_b$; in our simulations, typically $n_0/n_b = 10^{-3}$. Since we assume that the background number density n_0 is much larger than the number density of energetic particles n_b , the Maxwellian background represents an infinite reservoir and we can safely neglect any significant modification of f_T by the maser. Consequently, thermal Landau damping is time-independent and analytically calculated at the beginning of the simulation (see Eq. 8 below).

The energetic component, on the other hand, is of course modified by the maser. As outlined above, the initial distribution (Eq. 1) provides faster growth for lower-hybrid waves than

for any other (i.e. transverse) mode, provided that they are not suppressed by Landau damping (Eq. 8). According to Fleishman & Yastrebov 1994b, the dominance of the lower-hybrid mode is so strong that we consider in our quasilinear equations only the back-action from lower-hybrid waves on the energetic electrons. All other waves are considered in linear approximation, i.e. their growth and damping is calculated from the electron distribution modified by scattering on lower-hybrid waves.

Our model considers thus the temporal evolution of energetic electrons with distribution function

$$f(p, \mu, t), \quad f(p, \mu, t=0) = f_0(p, \mu) \quad (3)$$

(with f_0 given by Eq. 1) and of lower-hybrid waves with wave spectral energy density $W(k, \eta)$ per unit wave vector and unit volume,

$$W(k, \eta, t), \quad W(k, \eta, t=0) = W_{th}. \quad (4)$$

Here, the wave vector is parametrized by its modulus k and the direction cosine η relative to the magnetic field (so that $d^3\mathbf{k} = 2\pi k^2 dk d\eta$). As stated in Eq. (4), the initial wave spectral energy density is flat and equals the thermal level W_{th} .

Within quasilinear theory, the two distributions (Eqs. 3 and 4) evolve according to (Akhiezer et al. 1974, Melrose 1980, Fleishman 1994a)

$$\frac{\partial f}{\partial t} = \sum_{i,j} g_{ij} \partial_i D_{ij} \partial_j f \quad \text{with } i, j = p, \mu \quad (5)$$

$$\frac{dW}{dt} = (\Gamma^{QL} - \alpha)W \quad (6)$$

Here, Γ^{QL} is the growth/damping rate due to energetic electrons (Fleishman 1994a),

$$\Gamma^{QL}(k, \eta) = \frac{2\pi^2 \omega_p^2 \omega^2 n_b}{k^3} R(\eta) \sum_{n=-\infty}^{\infty} \int_0^{\infty} \frac{dp}{p|\eta|} J_n^2\left(\frac{k_{\perp} p_{\perp}}{\omega_{Be}}\right) \times \left(p \frac{\partial}{\partial p} + \left(\frac{k p \eta}{\gamma \omega} - \mu\right) \frac{\partial}{\partial \mu}\right) f \Big|_{\mu=(\gamma\omega - n\omega_{Be})/k p \eta} \quad (7)$$

and α is the Landau damping due to the Maxwellian background (Eq. 2)

$$\alpha = \sqrt{\frac{2}{\pi}} \frac{\omega_p}{\pi} \left(\frac{\omega_p}{c k \beta}\right)^3 e^{-\frac{1}{2} \left(\frac{\omega}{c k \beta \eta}\right)^2}. \quad (8)$$

$\beta (= v_{th}/c) = \sqrt{kT/mc^2}$. The diffusion coefficient $D_{\mu\mu}$ describes the resonant pitch angle scattering of electrons on lower-hybrid waves and has the form (Fleishman 1994a)

$$D_{\mu\mu}(p, \mu) = \frac{16\pi^3 e^2 \gamma^3}{m^2 p^5} \sum_{n=-\infty}^{\infty} \int_{-1}^1 d\eta \frac{\omega^2}{|\eta \mu|} \times \left(\frac{\gamma(1 - \mu^2) - n\omega_{Be}/\omega}{\gamma \mu}\right)^2 \times J_n^2\left(\frac{k_{\perp} p_{\perp}}{\omega_{Be}}\right) W(k, \eta) R(\eta) \Big|_{k=(\gamma\omega - n\omega_{Be})/p \eta \mu} \quad (9)$$

together with $g_{\mu\mu} = 1$ in Eq. (5), whereas for momentum-momentum diffusion we have

$$\frac{\partial f}{\partial t} = \frac{1}{p^2} \partial_p D_{pp} \partial_p f$$

with

$$D_{pp} = \frac{16\pi^3 e^2 \gamma}{m^2 p} \sum_{n=-\infty}^{\infty} \int_{-1}^1 d\eta \frac{\omega^2}{|\eta\mu|} J_n^2\left(\frac{k_{\perp} p_{\perp}}{\omega_{Be}}\right) \times \\ \times W(k, \eta) R(\eta) \Big|_{k=(\gamma\omega - n\omega_{Be})/p\eta\mu}. \quad (10)$$

Above, $p_{\perp} = p\sqrt{1 - \mu^2}$ and $k_{\perp} = k\sqrt{1 - \eta^2}$, $\gamma = \sqrt{1 + p^2/c^2}$ is the Lorentz factor, ω_{Be} is the electron gyrofrequency, ω_p is the electron plasma frequency, n_b and n_0 are the densities of fast and thermal electrons. The particle-wave resonance

$$\omega - k_{\parallel} v_{\parallel} + n\omega_{Be}/\gamma = 0$$

is taken into account by the conditions $|\mu=..$ and $|k=..$ in Eqs. (7), (9) and (10), respectively. J_n are Bessel functions, and $\omega = \omega(\eta)$ is the frequency of lower-hybrid waves as given by

$$\omega^2(\eta) = \frac{1}{2}(\omega_p^2 + \omega_{Be}^2) - \frac{1}{2}\sqrt{(\omega_p^2 + \omega_{Be}^2)^2 - 4\omega_p^2\omega_{Be}^2\eta^2}. \quad (11)$$

The quantity

$$R(\eta) = \left\{ \frac{\partial \omega \epsilon^l}{\partial \omega} \right\}_{\omega=\omega(\mathbf{k})}^{-1} \\ = \left[1 + \frac{\eta^2 \omega_p^2}{\omega^2(\eta)} + \frac{\omega_p^2}{\omega_{Be}^2} \frac{(1 - \eta^2)(1 + \omega^2(\eta)/\omega_{Be}^2)}{(1 - \omega^2(\eta)/\omega_{Be}^2)^2} \right]^{-1} \quad (12)$$

is a statistical weight, i.e. $R(\eta)$ is proportional to the volume in \mathbf{k} -space occupied by lower-hybrid waves with frequency between ω and $\omega + d\omega$. Alternatively, it can be interpreted as the fraction of the electric part of the total wave energy (Melrose, 1980).

2.1. Simplified model

In general, Eq. (5) describes both pitch-angle and momentum diffusion. However, the two contributions are expected to be of different order of magnitude for several reasons. Since the p -derivatives are always negative in f_0 (Eq. 1), the p -slope does not excite lh waves but provides damping. Amplification is entirely due to ∂_{μ} ; so we expect that quasilinear diffusion will mainly affect μ since it attempts to destroy the cause of wave growth. Of course, such a ‘Le Chatelier’ argument applies to any kind of losscone distributions and waves treated in previous studies as well, but there is another point which distinguishes the present case. From a quasi-particle point of view, the lower-hybrid photons carry relatively small energy $\hbar\omega$ per momentum, i.e. when compared to transverse photons. We expect thus that during the emission or absorption of lower-hybrid photons, the (scalar) change in the electron energy is small relative to the (directional) change in momentum, and that this is i.e. so when

compared to transverse photons. Thus, p -diffusion is expected to be less important relative to μ -diffusion for lh waves, than it is the case for transverse waves.

In the wave description, the dominance of pitch-angle diffusion manifests in the width of the factor $(\frac{k_{\parallel} p_{\parallel}}{\gamma\omega} - \mu)^2$ in Eq. (9) which, for our parameters, is in the order of 50...100 and is absent in p -diffusion (Eq. 10). In fact, when calculated from the initial wave energy density $W = W_{th}$, the momentum diffusion rate (defined below) is found to be 3 orders of magnitude smaller than the pitch angle diffusion rate. This suggests to neglect momentum diffusion against pitch-angle diffusion, at least at an initial stage. In order to investigate the relative order of momentum- and pitch angle diffusion at later times, we use a code where diffusion is restricted to the pitch-angle and numerically compare the momentum diffusion rate $(\frac{\partial f}{\partial t})_p = p^{-2} \partial_p D_{pp} \partial_p f$ to the pitch angle diffusion rate $(\frac{\partial f}{\partial t})_{\mu} = \partial_{\mu} D_{\mu\mu} \partial_{\mu} f$. We computed the average and maximum of $(\frac{\partial f}{\partial t})_p$ and $(\frac{\partial f}{\partial t})_{\mu}$, and considered the mean and maximum of the control quantity $Q \doteq \frac{|(\partial f/\partial t)_p|}{|(\partial f/\partial t)_{\mu}| > \epsilon}$ which characterizes the local ratio of momentum-to-pitch angle diffusion. ($\epsilon > 0$ in the denominator preserves from numerical noise and is small compared to $|(\partial f/\partial t)_{\mu}|$ during the phase where diffusion effectively takes place.) The results of a typical run are shown in Fig. 2. The average p -diffusion rate is at least 2 orders of magnitude smaller than the average μ -diffusion rate, and the same holds for their maxima. The average ratio $\langle Q \rangle$ is always below one percent, and the maximum of Q (representing that point in $p\mu$ -space where momentum diffusion is relatively most important) is almost always below 10 percent. Exceptions at $t \sim 2$ ms arise from isolated points in the $p\mu$ -grid. It was also found that $\partial_p f < 0$ for all times, so that the restriction to μ -diffusion does not create artificial positive p -slopes (whose correct relaxation would require the inclusion of p -diffusion). Finally, the question remains whether our results would also hold if p -diffusion was implemented in the code. This can be clearly answered by yes, because p -diffusion acts such as to decrease the p -diffusion rate. When p -diffusion was included in the dynamics, this should enhance the dominance of μ -diffusion.

Based on the above results and arguments, we conclude that momentum diffusion is negligible compared to pitch-angle diffusion in our situation. Our simplified model reads thus

$$\frac{\partial}{\partial t} f(p, \mu) = \frac{\partial}{\partial \mu} D_{\mu\mu}(p, \mu) \frac{\partial}{\partial \mu} f(p, \mu) \quad (13)$$

$$\frac{\partial}{\partial t} W(k, \eta) = \Gamma(k, \eta) W(k, \eta) \quad (14)$$

with initial conditions $f(p, \mu, 0) = f_0$ (Eq. 1) and a flat initial wave energy density $W(k, \eta, t = 0) = W_{th}$.

2.2. Properties of $D_{\mu\mu}(p, \mu)$ and Γ^{QL}

The diffusion coefficient $D_{\mu\mu}(p, \mu)$ for lh waves, calculated from the initial thermal wave spectrum $W(k, \eta) = W_{th}$, is shown in Fig. 1. First we notice that although the wave spectrum is flat, the diffusion coefficient is not but exhibits a peaky structure as a consequence of discrete resonances.

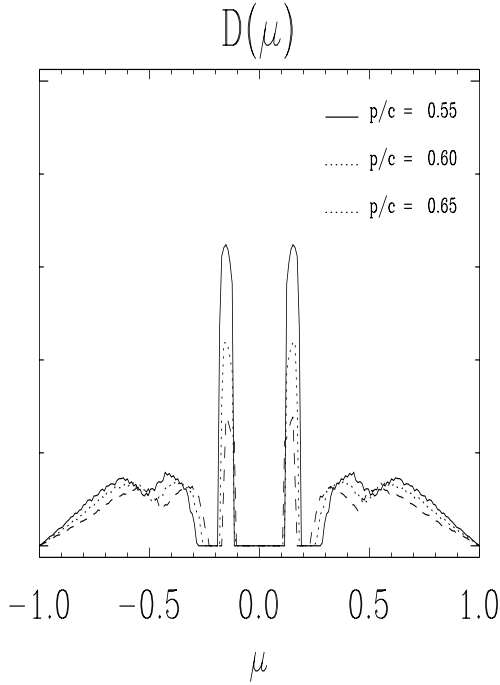


Fig. 1. The initial diffusion coefficient in dependence of μ for several values of p/c as created by a flat wave spectral energy density $W = W_{th}$.

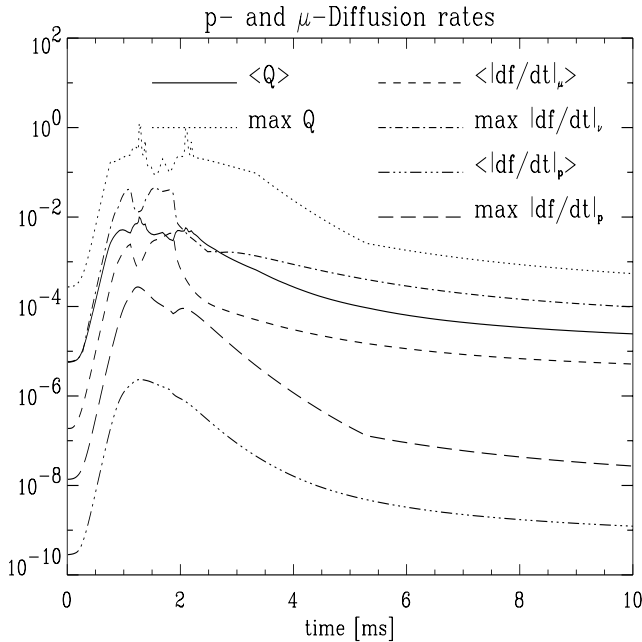


Fig. 2. The diffusion rates (see text) in units of ms^{-1} for pitch-angle and momentum-diffusion; the initial distribution being normalized to unity. The quantity Q is a local measure of relative strength of p - and μ -diffusion, $Q = |df/dt|_p / (|df/dt| + \epsilon)$, with $\epsilon = 5 \cdot 10^{-5} \text{ms}^{-1}$.

Secondly, we notice from Fig. (1) that the diffusion coefficient is symmetric in μ , $D_{\mu\mu}(p, \mu) = D_{\mu\mu}(p, -\mu)$. This can also be seen from Eq. (9), where the sign of μ affects only the resonance condition. Since $\omega(\eta)$ and $R(\eta)$ (Eqs. 11, 12) are

even functions of η , a change of sign $\mu \rightarrow -\mu$ can be compensated by a change of the integration variable $\eta \rightarrow -\eta$, without changing the value of the integral, provided that $W(k, \eta) = W(k, -\eta)$. Hence, an η -symmetric wave energy density yields a μ -symmetric electron diffusion coefficient, which is i.e. the case for the flat initial wave energy distribution $W(k, \eta) = W_{th}$. On the other hand, the growth rate Γ^{QL} is symmetric in η , $\Gamma^{QL}(k, -\eta) = \Gamma^{QL}(k, \eta)$ if the electron distribution is symmetric in μ , $f(p, \mu) = f(p, -\mu)$. This follows from Eq. (7) by a simultaneous change of signs of η and μ . Therefore, if the initial system has the symmetry $f(p, -\mu) = f(p, \mu)$ and $W(k, -\eta) = W(k, \eta)$, it will preserve this symmetry for all times. We shall make use of this property in our numerical implication.

Thirdly, we point out that $D_{\mu\mu}(\mu = 0) = 0$. Due to the resonance condition, $\mu = 0$ corresponds to $k = \infty$ and since there are no photons of arbitrary large momentum, the diffusion coefficient vanishes¹. Hence, there is no diffusion at $\mu = 0$ and the initial anisotropy can *not* vanish. We should note at this point that $D_{\mu\mu}(\mu = 0) = 0$ is a special feature lh waves and is not true for transverse waves. The difference stems from the different resonance behaviour of lh and transverse waves at $\mu = 0$ ($v_{\parallel} = 0$). As for lh waves $\omega \ll \omega_{Be}$ (or at least $\omega < \omega_{Be}$), the resonance condition $k_{\parallel}v_{\parallel} - \omega - n\omega_{Be}/\gamma = 0$ is only satisfied for $\gamma \gg 1$ – and such ultra-energetic particles are not present in our model. Hence, there is no diffusion on lh-waves at $\mu = 0$. In contrast, transverse waves may have $\omega \geq \omega_{Be}$ and resonance occurs with mildly energetic particles (e.g. Aschwanden 1990b, Eq. 20 and Fig. 7).

Qualitative behaviour of quasilinear relaxation. The initial and final stages of quasilinear relaxation are well known (Akhiezer et al. 1974). In the very beginning of the process, the waves growth exponentially and the electron distribution does not change (linear stage). At later times when the wave spectral energy density becomes large, the electron distribution is modified in a quite complicated way. At the end of the relaxation process, there are two possible final states: either $\Gamma = 0$ or $W = 0$. The former requires a plateau formation in the electron distribution and is less likely to occur. The exact behaviour of $W(k, \eta)$ and $f(p, \mu)$ during relaxation (as well as the choice of the final state) depends on specific conditions and must be investigated numerically.

3. Numerical code

Dimensionless variables. Within our code, the physical variables ω, p, k, t are treated in a dimensionless form, where the

¹ More precisely, we must consider the limit $\mu \rightarrow 0$ of Eq. (9). Within the semi-classical framework of quasilinear theory, $W(k, \eta)$ is a continuous function of k and the request of finite (total) energy implies only that $\int W(k) E(k) dk < \infty$. However, the underlying quantum mechanical description demands finite energy for every photon, and this provides a truncation of $W(k, \eta)$. As a consequence, $D_{\mu\mu}(|\mu| \leq \mu_{min}) = 0$ which mathematically ensures that there is no diffusion at $\mu = 0$.

frequency is normalized by $\omega' = \omega/\omega_p$, momentum is normalized by $p' = p/c = \gamma v/c$, wave vector is normalized by $k' = kp_0/\omega_{Be}$ and time is normalized by the gyrotime, $t' = t\omega_{Be}$. As a consequence of the latter, the assignment of physical time units requires an assumption on ω_{Be} . We shall use $f_{Be} = 1$ GHz.

Numerical grid. We perform a numerical (time domain) integration of the quasilinear Eqs. (13, 14). In this, the distributions $f(p, \mu)$ and $W(k, \eta)$ are defined on regular grids in (p, μ) - and (k, η) -space. The choice of regular grids is motivated by the attempt of finding multiple peaks, which could be looked over when concentrating on a specific region with high local resolution. In order to resolve the integrands in Eqs. (7) and (9), a grid size of $> 50 \times 50$ data points is necessary. When choosing the particle grid (p, μ) , we take into account that our initial distribution f_0 (Eq. 1) is flat at $p < p_0$. Thus, this part does not contribute any derivatives and does not affect the growth rate, nor could diffusion take place. We can therefore restrict our grid to $p \geq p_0$. Similarly, very large momenta $p \gg p_0$ will not yield any significant derivatives, since the whole distribution decays with $p^{-\xi}$. We can therefore restrict our grid also to $p < p_1$, with p_1 such that $f(p_1, \eta) \ll f(p_0, \eta)$. We chose $p_0 = 0.54$ and $p_1 = 1.1$ for $\xi = 5$. Concerning the angular variable μ , its full allowed range is $-1..1$; if, for some grid points, $\mu_{res} = (\gamma\omega - n\omega_{Be})/k\eta p$ (Eq. 7) is outside $-1..1$, this means that the resonance condition cannot be satisfied. We suppress such cases by setting $f(|\mu| > 1) = 0$ in our code.

For the wave grid (k, η) , η covers again the full range of angles $-1..1$, and for k we can restrict our calculations to values where waves effectively are amplified: for large k ($k > k_{max}$), Landau damping on thermal electrons dominates, and for small k ($k < k_{min}$), the phase velocity of waves is larger than the speed of light, so these waves can not be generated by particles. For our parameters, $k_{min} = \omega_{Be}/p_0$ and $k_{max} = 3.5 \omega_{Be}/p_0$.

Calculation of $\Gamma(k, \eta)$ and $D_{\mu\mu}(p, \mu)$. For the efficient numerical evaluation, we write Eqs. (7) and (9) in the form

$$\begin{aligned} \Gamma_{ij} &= K_{ijlm}^\Gamma f_{lm} \\ D_{ij} &= K_{ijlm}^D W_{lm}. \end{aligned}$$

The kernels K^D and K^Γ , which involve special function calls, are computed and stored once, so that the calculation of $D_{\mu\mu}(p, \mu)$ and $\Gamma(k, \eta)$ reduces to a computationally fast (sparse) tensor multiplication. The temporal benefit of the method is considerable; on our workstation and using a grid of $f \sim 60 \times 60$, the time needed for one tensor multiplication is a few seconds, whereas a straightforward calculation of $D_{\mu\mu}(p, \mu)$ and $\Gamma(k, \eta)$ by DO-loops over η and p (Eqs. 7 - 9) and repeated special function calls would take 20 minutes.

The calculation of the kernels K^Γ and K^D follows a discretized version of Eqs. (7) and (9), with p and η integration variables defined on the regular grids. As the resonance condition occurs in general between the grid points, the resonance values have to be interpolated. We use a bilinear interpolation for

$W(k, \eta)$ and a higher-order spline for $f(p, \mu)$, accounting for derivative evaluation (Eq. 7). The numerical integrations over p and η are performed by an elementary Simpson routine.

Updating $f(p, \mu)$. The pitch angle diffusion (Eq. 13) is discretized by the Crank-Nicholson scheme (Press et al. 1989, Hamilton et al. 1990) which ensures stability of the numerical diffusion process. It consists of the following implicit equation for the updated distribution f^{n+1}

$$\begin{aligned} \frac{f_i^{n+1} - f_i^n}{\Delta t} &= \frac{1}{2(\Delta x)^2} \left[D_{i+\frac{1}{2}}(f_{i+1}^n - f_i^n) - D_{i-\frac{1}{2}}(f_i^n - f_{i-1}^n) \right. \\ &\quad \left. + D_{i+\frac{1}{2}}(f_{i+1}^{n+1} - f_i^{n+1}) - D_{i-\frac{1}{2}}(f_i^{n+1} - f_{i-1}^{n+1}) \right] \quad (15) \end{aligned}$$

with $f_i^n = f(p, \mu_i, t_n)$, $D_i = D(\mu_i)$ ($i = 1..N$, p fixed), and $D_{i\pm\frac{1}{2}} = \frac{1}{2}(D_i + D_{i\pm 1})$.

μ -Boundary conditions. As it stands, Eq. (15) is not complete yet but requires the definition of boundary conditions at $i = 0$ and $i = N + 1$. To this end, we worked out two cases depending on the degree of symmetry of the system.

I) We first note that, due to the parametrization by μ , we introduce a symmetry $\alpha \leftrightarrow -\alpha$ with α the pitch angle. This symmetry suggests that the continuation of $f_i = f(\mu_i)$ out of the unique definition range $i = 1..N$ must follow the corresponding continuation of $f_\alpha(\alpha_i)$, implying $f_0 = f_2$ and $f_{N+1} = f_{N-1}$ if the boundaries $-1, 1$ are on the grid; and $f_0 = f_1$ and $f_{N+1} = f_N$ if the boundary points are centered between the grid points. The latter possibility is preferable since it ensures strict conservation of particle number, as can be seen by summing up the righthand side of Eq. (15) over $i = 1..N$. We shall therefore use a grid which is interlaced with respect to the boundary points, and set $f_0 = f_a$ and $f_{N+1} = f_N$ for situations with $f(p, \mu) \neq f(p, -\mu)$, which is required for the comparison with existing calculations (see below).

II) Apart of this, our initial distributions (Eqs. 1, 4) are symmetric in μ and η . According to Sect. 2.2, this symmetry is preserved for all times, so that we have an additional symmetry about $\alpha = 90^\circ$. Together with the symmetry about $\alpha = 0$, this implies that $f(\mu_{N+1}) = f(\mu_0)$ and we can impose cyclic boundary conditions for f_i . Similarly, we set $D_{N+\frac{1}{2}} = D_{\frac{1}{2}}$. As a – desired – consequence of periodic boundary conditions, the electron number is numerically conserved, like for case (I) treated above. To see this, we sum again up both sides of Eq. (15) over $i = 1..N$. The righthand side vanishes since it contains terms of the form

$$\sum_{i=1}^N \left[D_{i+\frac{1}{2}} \delta f_{i+\frac{1}{2}}^n - D_{i-\frac{1}{2}} \delta f_{i-\frac{1}{2}}^n \right] = 0$$

with $\delta f_{i\pm\frac{1}{2}}^n = \pm(f_{i\pm 1}^n - f_i^n)$ and similar for f^{n+1} ; the above sum vanishes because of the periodicity of the summands. Hence, the lefthand side of Eq. (15) must also vanish (for every p) – ensuring numerical conservation of the electron number.

The introduction of periodic boundary conditions into the implicit Crank-Nicholson scheme (Eq. 15) is somewhat more subtle than in explicit schemes and requires a special method described in A. It was verified that the two boundary conditions (I) and (II) lead to the same result if $f(p, \mu)$ and $W(k, \eta)$ are symmetric in μ and η .

Sum over harmonics. The infinite sum over n -th harmonics (Eqs. 7, 9) was truncated at $n = \pm 3$. Higher numbers contribute less, which was checked numerically.

Updating $W(k, \eta)$. The time updating of the wave field is performed according to the explicit scheme

$$W(t_{n+1}) = W(t_n) e^{\Gamma(t_n)\Delta t}$$

which corresponds to the analytical solution $W(t) \propto \exp(\int_0^t \Gamma(t') dt')$ of Eq. (14) and ensures positivity and better accuracy than a linearized form. Wave densities below W_{th} were set to W_{th} , corresponding to a temperature of $T = 10^6$ K or $\beta = 0.01$, respectively.

3.1. Test of the code

Growth and diffusion coefficients. In a first test, we compared the growth-and diffusion coefficients obtained by our code with comparable values from existing literature (Fleishman & Yastrebov 1994b)

Grid resolution. The grid resolution was increased to see the dependence of our results on the cell size; it was found that the principal features summarized below are not affected by the resolution if this was sufficient to resolve the diffusion coefficient (Fig. 1).

Time updating. Our Crank-Nicholson implementation was also tested against an explicit code with smaller time steps (satisfying the Courant condition), and it was found that they agree. In addition, different integration schemes (primitive summation, Simpson, Runge-Kutta, Rhomberg) were used for Eqs. (7),(9) and checked for numerical agreement.

Particle number conservation. The cyclic Crank-Nicholson code enforces exact particle number conservation, $\int p^2 dp \int d\mu f(p, \mu) = const.$

Energy and momentum conservation. Total (electrons plus wave) energy is not conserved because we neglect the derivatives ∂_p in the diffusion equation. Generally, total momentum is not conserved. However, it is exactly conserved when we consider situations which are symmetric in μ and η , where the total momentum is zero. The lack of energy conservation however is a drawback of our code, since it does not allow to use energy conservation as a consistency check.

Comparison with existing calculations In order to compare our results with existing calculations, we chose an initial situation of the form used by Aschwanden & Benz 1988, Aschwanden 1990b. The Maxwellian of temperature $T_h = 100 T_b$ and is multiplied by a one-sided losscone modeled by $g(\alpha) = \sin^6(\alpha/\alpha_c \pi/2)$ if $\alpha \leq \alpha_c$ and $g(\alpha) = 1$ if $\alpha > \alpha_c$. We chose $\alpha_c = \pi/4 = 45^\circ$, which is somewhat wider than Aschwanden's choice ($\alpha = 30^\circ$) but is better resolved in our regular μ -coordinates. In our coordinates, and using the amplifying side of the ambiguous distribution $f(\mu) = f(\alpha^2)$, this becomes

$$g^*(\mu) = \begin{cases} 64\mu^6(1-\mu^2)^3 & \mu < -1/\sqrt{2} \\ 1 & \text{else} \end{cases} \quad (16)$$

where normalization is such that $g(\alpha) \sin \alpha d\alpha = g^*(\mu) d\mu$. Note that the initial distribution (16) is not symmetric in μ ; we therefore use nonperiodic boundary conditions, as described in alternative (I) above. The initial wave energy density is flat $W(k, \eta) = W_{th}$, like in Aschwanden's study (Aschwanden 1990b).

The result of our calculation is shown at the lefthand side of Fig. 3, whereas the outcome of the simulation with our two-sided losscone (Eq. 1) is shown on the right of Fig. 3. Both runs were performed with the identical program, i.e. using nonperiodic boundary conditions. As can be noticed, the Aschwanden-type losscone (left) almost completely relaxes and the final electron distribution becomes almost isotropic, whence the wave energy density shows a simple, single-peaked structure. This result is in agreement with the traditional picture of quasilinear relaxation (Aschwanden 1990b, Wu et al. 1981, Pritchett 1986). On the other hand, the initial distribution of Eq. (1) (right) remains clearly anisotropic after relaxation. This is because some of the relevant anisotropy occurs at values of $\mu \approx 0$ where the diffusion coefficient vanishes (due to impossible resonance condition, see Sect. 2.2.) Although Aschwanden and others (Aschwanden 1990b, Wu et al. 1981, Pritchett 1986) considered the relaxation on different waves, we find thus a general agreement with our code if we use a $\sin^N \times$ Maxwell initial conditions. We interpret this as an indicator for the reliability of the code and the approximations made in its derivation.

4. Simulations and initialisation

We performed numerous runs with varying physical parameters of the initial electron distribution and did not find a distinct dependence of our results on the initial parameters, or any simple rule to predict the temporal evolution of the wave spectral energy density. Landau damping can suppress the instability of lower-hybrid waves (Eq. 17). In this case, other modes (X or Z) will dominate which are not treated in the present study (see Aschwanden 1990b, Fleishman & Yastrebov 1994b). In the following, we discuss one representative example where our model applies.

Choice of initial parameters. Initial amplification of lower-hybrid waves occurs when the amplifying contributions of the

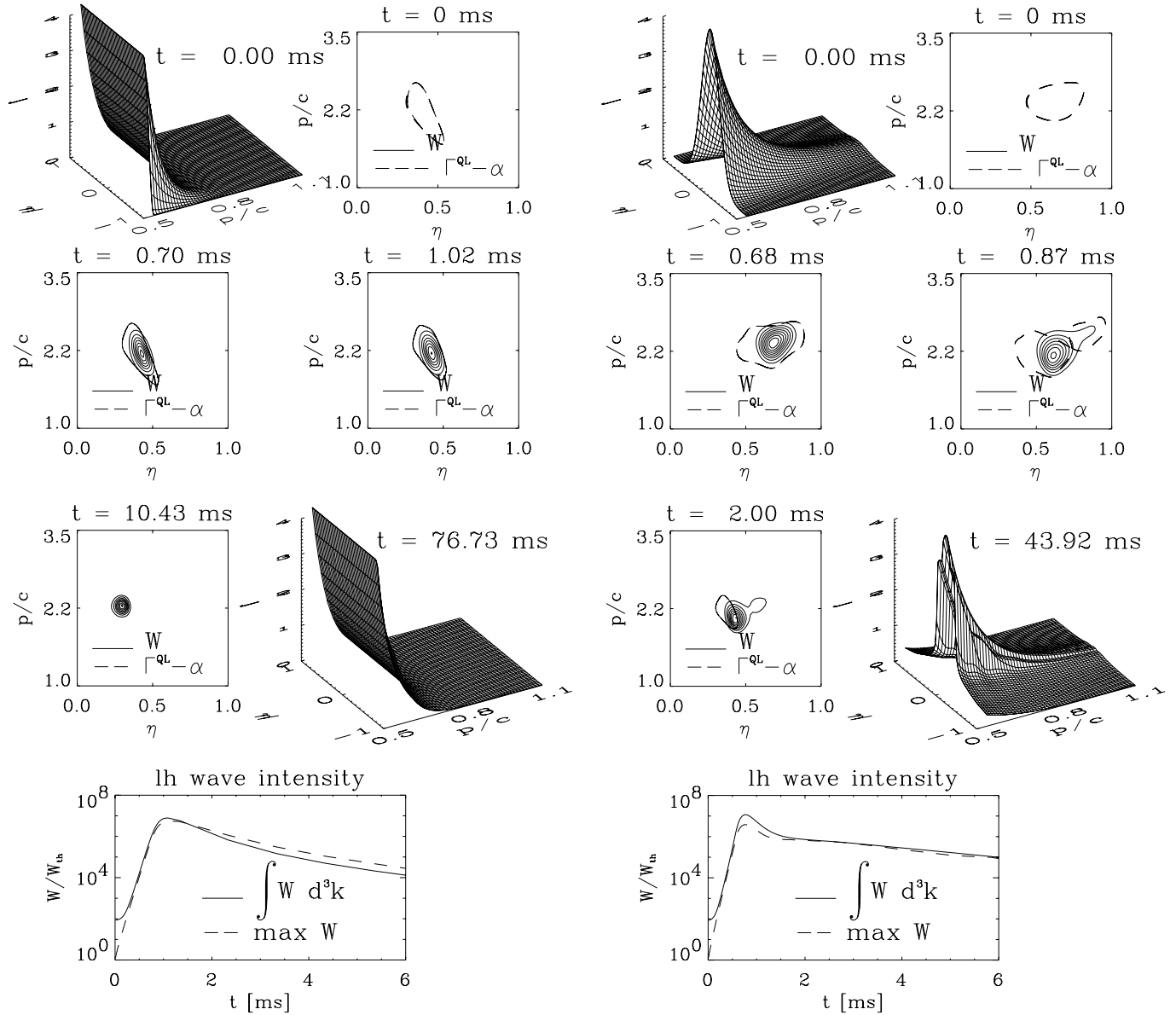


Fig. 3. Comparison of our lower-hybrid code with existing calculations on transverse-wave relaxation. Left: a one-sided losscone modeled by a $\sin^N \times$ Maxwell initial distribution (Aschwanden 1990b, see Eq. 16). Right: the two-sided losscone (f_0 , Eq. 1) considered in this paper. Note that the narrow one-sided Maxwellian losscone becomes almost isotropic, but the broader two-sided losscone with powerlaw energy spectrum does not. Both figures were created by the same program, using noncyclic boundary conditions (I, Sect. 3).

derivatives $\partial_\mu f$ in Eq. (7) dominate against the damping contributions of $\partial_p f$ and the Landau damping (Eq. 8); for the powerlaw distribution (Eq. 1), this requires that

$$\frac{p_0}{c} \frac{\omega_{pe}}{\omega_{Be}} > C(\xi, \mu_0) \sqrt{T/10^6 \text{K}} \quad (17)$$

(V.B.Korsakov 1997). For example, for $\xi = 4$ and $\mu_0 = 0.33$, we find $C(4, 0.33) \approx 0.2$. The initial wave spectral energy density was assumed as flat, $W(k, \eta) = W_{th} = \text{const}$. The detailed shape of the initial wave spectral energy density is not of great importance, since the amplification is by many orders of magnitude and at $t \gg t_{linear}$, $W(k, \eta)$ is dominated by the amplification process rather than by the initial state. The

initial electron distribution is given by Eq. (1) with $\xi = 5$, $p_0 = 0.54 \times c$ and $p_1 = 1.1 \times c$, the fraction of fast electrons is $n_b/n_0 = 10^{-3}$ and the gyrofrequency is $f_{Be} = 1$ GHz. The latter determines the physical time scale ($\sim 1/\omega_{Be}$) and was chosen with regard to observations (see below).

5. Results

The main results of our calculations are illustrated in Figs. 4 and 5 which show the evolution of the fast electron distribution $f(p, \mu)$ and wave spectral energy density $W(k, \eta)$, together with the diffusion coefficient $D_{\mu\mu}(p, \mu)$ and growth rate $\Gamma(k, \eta)$ of lower-hybrid waves.

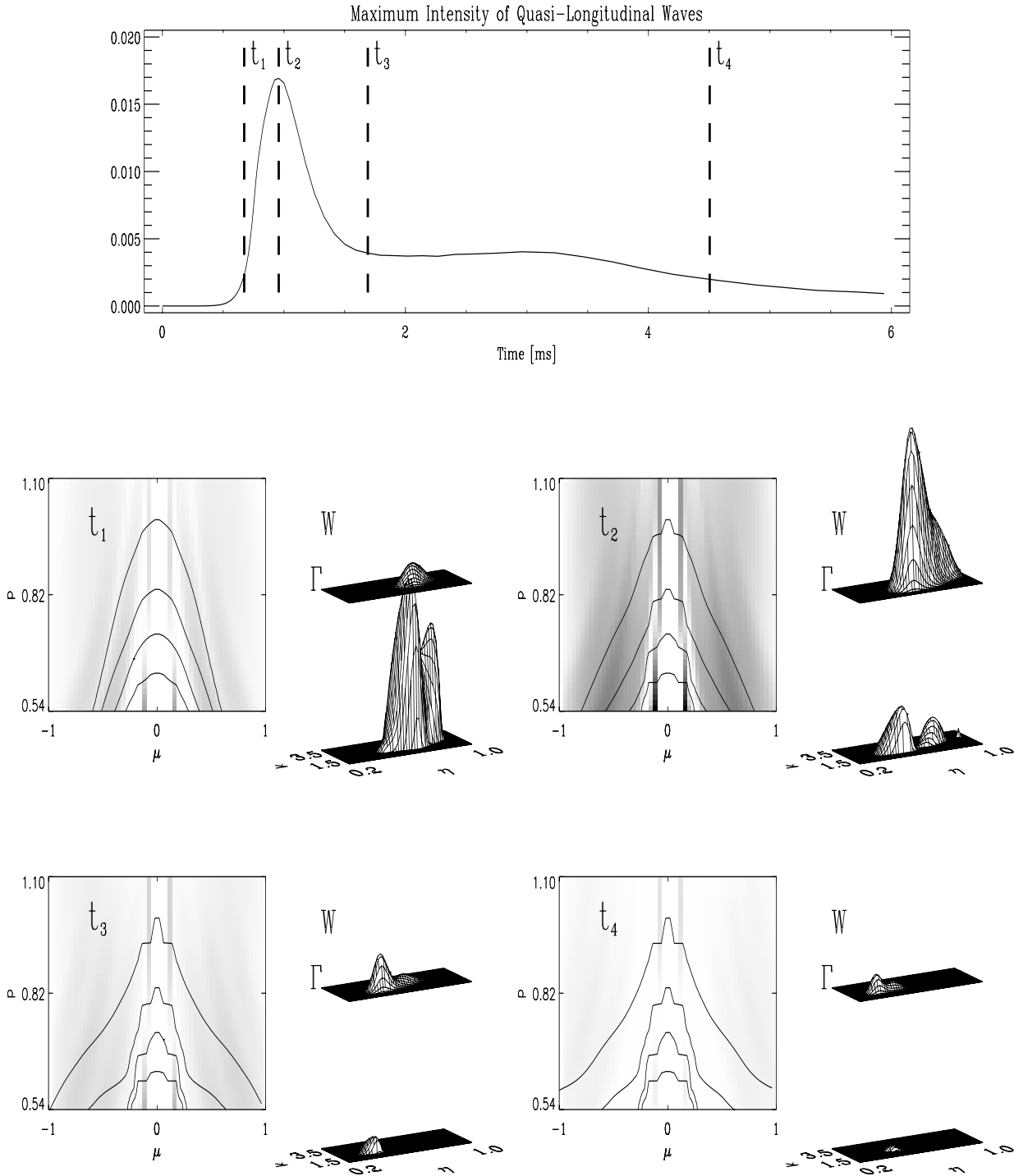


Fig. 4. The time evolution of a quasilinear maser driving lower-hybrid waves. Top: time evolution of the maximum lower-hybrid wave spectral energy density. Bottom 4 figures: time cuts at t_1 to t_4 . Left: electron distribution (relative contours: 0.2, 0.5, 1, 2) and diffusion coefficient (grayscale). Right: Plasma wave spectral energy density (top) and positive part of the amplification rate (below). See also Fig. 5. These results, which refer to a symmetric situation $\mu \leftrightarrow -\mu$, were obtained using periodic boundary conditions (II, Sect. 3).

In Fig. 4, the top graph shows the time evolution of the maximum of $W(k, \eta)$. The four subsequent graphs represent snapshots of $f(p, \mu)$ (contours), $D_{\mu\mu}(p, \mu)$ (grayscale), $W(k, \eta)$ and the positive part of $\Gamma(k, \eta)$. The evolution of the electron distribution is shown in more detail in Fig. 5 which shows cuts

of $f(p, \mu)$ at constant p for subsequent times, together with $D_{\mu\mu}(p, \mu)$, $\Gamma(k, \eta)$ and $f(p, \mu)$.

Note that the shape and value of the growth rate start to change when the value of wave spectral energy density is much lower than its peak value. This results in slower wave growth

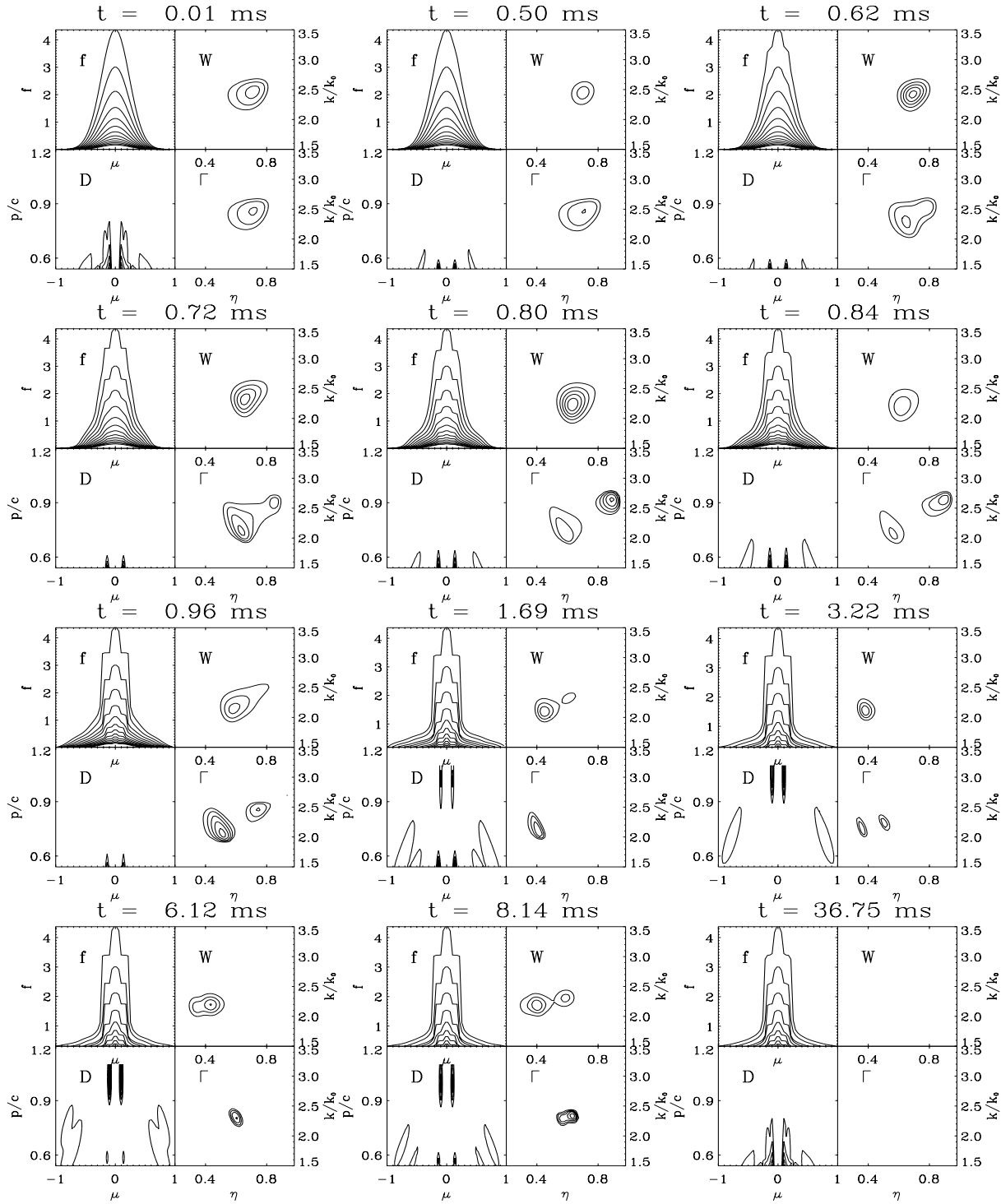


Fig. 5. Same situation as in Fig. 4. Cuts through the electron distribution function at $p/c = 0.54, 0.58, 0.62, \dots$ (top to bottom), together with $\Gamma(k, \eta)$, $D_{\mu\mu}(p, \mu)$ and $W(k, \eta)$. Note the plateau formation in $f(p, \mu)$ occurring where $D_{\mu\mu}(p, \mu)$ is large and the appearance of several peaks in $\Gamma(k, \eta)$, followed by corresponding peaks in $W(k, \eta)$. After relaxation, the lower-hybrid waves fall back to the level W_{th} and the diffusion coefficient $D_{\mu\mu}(p, \mu)$ equals the initial one. See also Fig. 4

than the exponential one expected from the linear theory. Simultaneously, the electron distribution becomes more isotropic. The modification of the electron distribution occurs in regions where $D_{\mu\mu}(p, \mu)$ is large and proceeds to the extent sufficient to provide damping of the initially unstable waves. However,

the resulting electron distribution can provide instability at regions of the k -space which were initially stable. In this case we see the appearance of subsequent, partially overlapping peaks in the wave spectral energy density $W(k, \eta)$ (Fig. 5) which also manifest in the tail of the time profile of $\max(W)$ (Fig. 4 top).

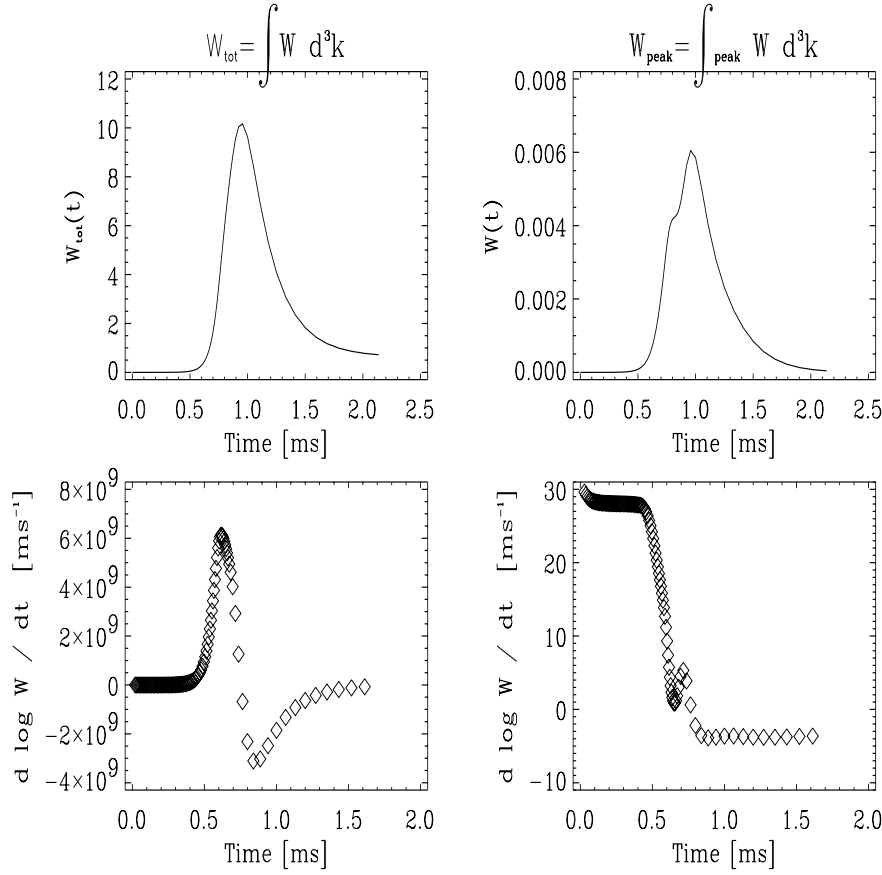


Fig. 6. The temporal evolution of the first peak in Fig. 4 in the total lower-hybrid wave energy (left) and the lower-hybrid wave spectral energy density integrated over the region of the initial peak (right). The scaling of physical time corresponds to $\omega_{Be} = 1$ GHz. Below, the logarithmic derivatives are shown which allow a clear distinction between linear ($d \ln W / dt = \text{constant}$) and nonlinear ($d \ln W / dt \neq \text{const}$) regimes. Note that the initial growth rate is about 30 ms^{-1} which corresponds to growth time of 0.033 ms . The nonlinearities onset after 0.5 ms , thus after ~ 15 growth times.

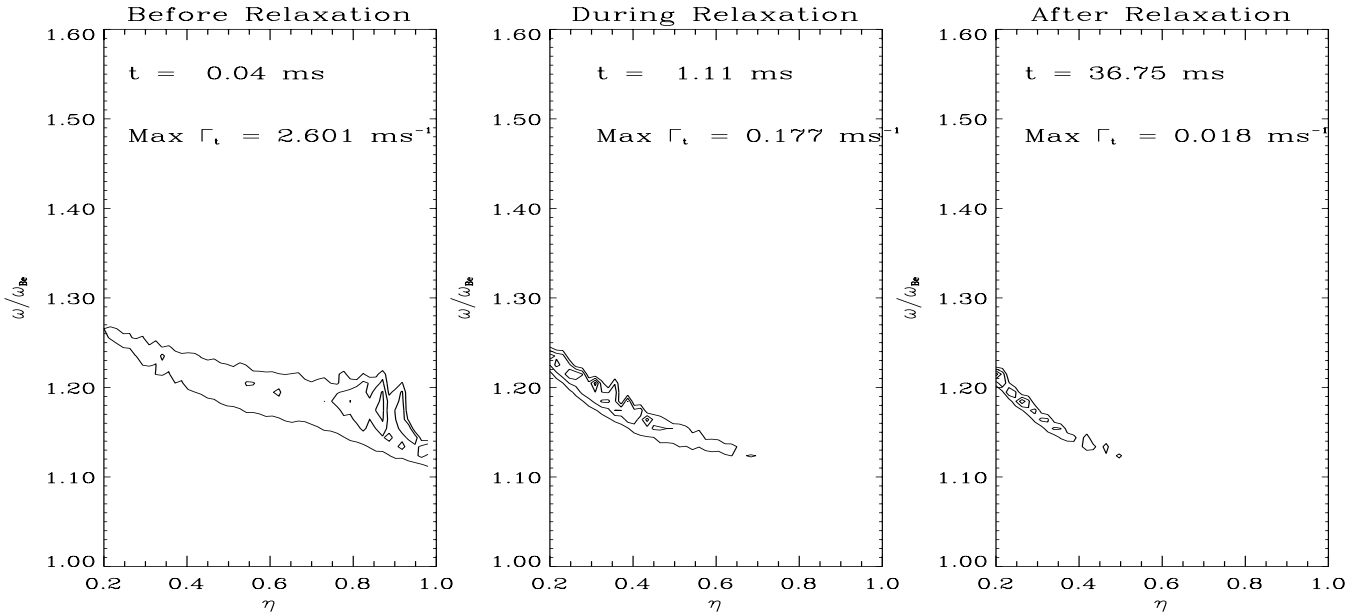


Fig. 7. The positive part of growth rate for transverse waves ($\Gamma_t > 0$) before, during and after relaxation due to lower-hybrid waves. Although the relaxation diminishes Γ_t , this is still positive in some regions where, in a second stage, maser amplification of transverse waves can occur.

After relaxation, the electron distribution does not completely isotropize. Therefore, scattering on lower-hybrid waves does not provide a very efficient isotropization mechanism. The final distribution is isotropic only to the extent as to

be stable respective to waves included in our relaxation code. Contrary, the waves which were not included (e.g., transverse X and O waves) remain unstable (see Fig. 7) since they are driven by other fractions of the fast electrons.

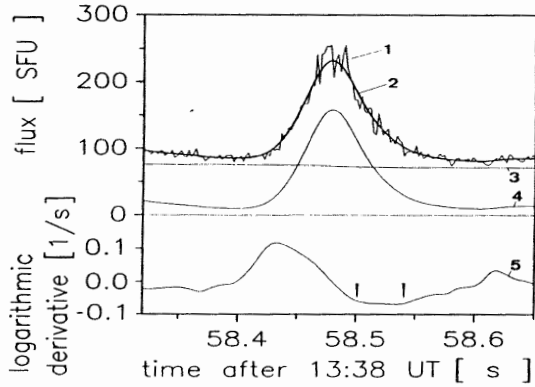


Fig. 8. Observed intensity profile at 360 MHz. 1: raw data, 2: smoothed, 3: background, 4: background subtracted, 5: logarithmic derivative. Courtesy from Güdel & Benz 1990

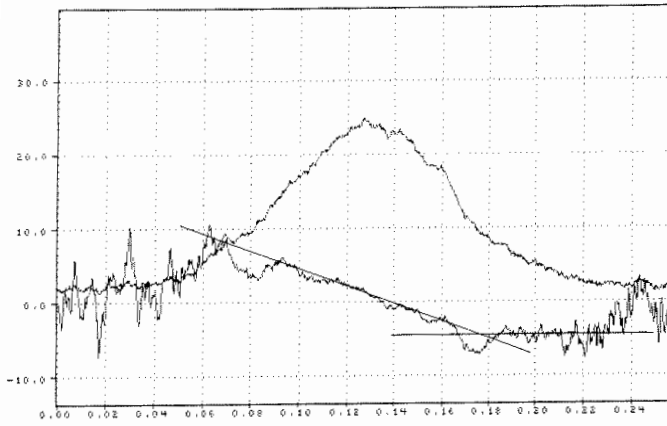


Fig. 9. Another burst profile observed at 540 MHz, together with its logarithmic derivative. For comparison, a straight line is superimposed which shows the almost Gaussian behaviour of the peak region. Courtesy from Melnikov et al. 1999

Fig. 6 presents the dependence of the total (left) and initial peak (right) wave energy of lower-hybrid waves on time, together with their logarithmic derivatives. The total wave energy is the spectral wave energy density $W(k, \eta)$ integrated over all wave vectors; the initial peak wave energy is $W(k, \eta)$ integrated over the region where the initial growth rate is larger than 5 percent of its maximal value and represents the initial peak region. The logarithmic derivative (\sim the growth rate) was chosen since it allows the clear distinction from linear maser features: the flat parts of the curve correspond to exponential growth or decay of waves (linear regime). In order to assign a physical timescale to the normalized code time units, we have to prescribe the electron gyro frequency. In Figs. 6 and 7, we assume $f_{Be} = 1$ GHz; more generally, the physical time scales with f_{Be}^{-1} . Note that the initial peak growth rate is about 30 ms^{-1} corresponding to a growth time of 0.033 ms , and that the linear regime of the initial peak (Fig. 6 right) is left after 0.5 ms , so that nonlinear effects onset after ~ 15 growth times. Due to subsequent peaks however, the relaxation of the whole system (all wave vectors) takes much longer, namely about 5 ms as can be noticed from Fig. 4 top.

Despite the complicated, multi-peaking evolution in k -space, we emphasize the quite simple shape of the peak in the *integrated* wave spectral energy density, consisting of a Gaussian rise phase (from $\sim 20\%$ of the peak value to $\sim 80\%$ at decay) and an exponential decay phase (after 80% of the maximum value). This finding fits well the observed shape of single spikes (Güdel & Benz 1990, Fig. 8; Melnikov et al. 1999, Fig. 9). We suggest thus that the Gaussian rise phase is a signature of quasilinear relaxation in the spike source. One should also notice that nonlinear plasma emission – which is currently considered as alternative mechanism to ECM – provides substantially different time profiles characterized by an exponential rise and decay in oscillating, quasi-periodic regimes and more complicated shapes in an irregular (spike-like) regimes (Korsakov & Fleishman, 1998, Fleishman & Korsakov, 1999).

Fig. 7 shows the growth rate for transverse waves (for the definition see Fleishman 1994a) in dependence of η and ω/ω_{Be} before (left), during (middle) and after (right) relaxation on lower-hybrid waves. The electron distribution function is taken from the same run as Figs. 4-6; the gyrofrequency (giving the physical time scale) is again 1 GHz . Note that the relaxed electron distribution still can amplify transverse waves in some restricted region of the (ω, η) -parameter range, although the growth rate is reduced when compared to the initial one. Note also that the maximal initial transverse growth rate Γ_t is by one order of magnitude smaller than for lower-hybrid waves (Fig. 6).

6. Summary and discussion

We performed a numerical study on the quasilinear relaxation of anisotropic fast electrons, amplifying and being pitch angle-scattered on lower-hybrid waves. The main findings of the study are the following.

1. The temporal evolution of the energy density of the fastest growing mode can peak at subsequent times.
2. The particle distribution remains clearly anisotropic during and after relaxation.
3. The final electron distribution is stable with respect to (initially) the fastest growing mode, but can still amplify other modes.
4. The characteristic saturation time (for a single peak) is of order of 15 inverse growth rates – in qualitative agreement with existing calculations – but the relaxation time of whole system (all wave vectors) is considerably longer.
5. The rise phase of the wave spectral energy density fits to Gaussian (not exponential) law, in agreement with spike observations.

The main difference to existing calculations is the possibility of multiple peaks. Their occurrence requires an initially non-flat μ -distribution at $\mu \ll 1$, where the initial diffusion coefficient has a complicate, peaky structure (Fig. 1). It is then possible that the first peak in $W(k, \eta)$ affects the electron distribution $f(p, \mu)$ only in a narrow (resonance) range and that this very localized diffusion does not relax possible further amplifying regions ($(k\eta p/\gamma\omega - \mu)\partial_\mu f > 0$). The presence of further am-

plifying regions in $p\mu$ -space is favoured by a broad energetic distribution such as a powerlaw used in the present study. (See i.e. Fig. 5, where a second diffusion region at large p occurs at $t > 1$ ms.) If further amplifying regions are present, they will relax as well, but with a lower efficiency, and their saturation can take place after the first amplifying region has relaxed. In this case, distinct peaks in the wave energy density appear.

The fact that scattering on lower-hybrid waves does not necessarily provide an efficient isotropization has some implications on precipitation models (e.g. Melnikov & Magun 1998) where it seems correct to neglect lower-hybrid wave scattering compared with Coulomb collisions.

We feel that future investigations on the quasilinear ECM are necessary, involving i.e. the back-action of transverse waves and the use full derivatives (∂_μ and ∂_p) in the model equations. Moreover, it is planned to include nonlinear effects (Fleishman 1994a) in our numerical code, which have so far only been studied in a qualitative way.

Acknowledgements. We thank M. Güdel and A. Benz (ETHZ, Switzerland) and V. Melnikov (NIRFI, Russia) for observational spike data, M. Aschwanden (Maryland, USA) for helpful discussions and A. Magun (IAP Bern, Switzerland) for supporting this collaboration. This work was partially supported by the Swiss National Foundation and the Russian Foundation of Basic Research under grant Nr. 97-02-16972.

Appendix A: numerical implementation of the cyclic Crank-Nicholson scheme

Contrary to the non-periodic boundary conditions (I, Sect. 3) which do not alter the tridiagonal form of the implicit equation (15), the introduction of periodic boundaries requires a modification of the usual tridiagonal solution scheme (e.g. Press et al. 1989). Since this might be of broader applicability, we give here a detailed description. We proceed as follows: with periodic boundaries, the Crank-Nicholson scheme (15) becomes

$$Mf^{n+1} = (2 - M)f^n \quad (\text{A.1})$$

with

$$M = \delta_{ij} + \chi \begin{pmatrix} D_{\frac{1}{2}} + D_{\frac{3}{2}} & -D_{\frac{3}{2}} & & -D_{\frac{1}{2}} \\ -D_{\frac{3}{2}} & D_{\frac{3}{2}} + D_{\frac{5}{2}} & -D_{\frac{5}{2}} & \\ & -D_{\frac{5}{2}} & \ddots & \ddots \\ -D_{\frac{1}{2}} & & & \ddots \end{pmatrix} \quad (\text{A.2})$$

with $\chi = \frac{\Delta t}{2(\Delta x)^2}$. Since M is not tridiagonal, we cannot use the standard algorithm given by Press et al. 1989, but introduce the following modification: due to its symmetry, M can be written as $M = U^T U$ where U is of the (upper triangular) form

$$U \doteq \begin{pmatrix} d_1 & b_1 & & X_1 \\ & d_2 & b_2 & X_2 \\ & & d_3 & b_3 & \vdots \\ & & & \ddots & \ddots & X_{N-2} \\ & & & & d_{N-1} & b_{N-1} \\ & & & & & d_N \end{pmatrix}.$$

Then,

$$M = \begin{pmatrix} d_1^2 & d_1 b_1 & & d_1 X_1 \\ d_1 b_1 & b_1^2 + d_2^2 & \ddots & b_1 X_1 + d_2 X_2 \\ & d_2 b_2 & \ddots & b_2 X_2 + d_3 X_3 \\ & & \ddots & \vdots \\ d_1 X_1 & b_1 X_1 + d_2 X_2 & \dots & b_{N-1}^2 + d_N^2 + \sum_{k=1}^{N-2} X_k^2 \end{pmatrix}$$

from which $d_1, b_1, X_1; d_2, b_2, X_2$ etc. are determined successively by comparison with Eq. (A.2). Eq. (A.1) is of the form $Mx = y$ and to be solved for x ; this is carried out in two steps: by setting $z = U^{-T}y$ and $x = U^{-1}z$, each of which is easily performed by forward/backward substitution. It turned out that additional stabilization such as pivoting is not needed in our application.

References

- Akhiezer A.I., Akhiezer I.A., Polovin R.V., Sitenko A.G., Stepanov K.N., 1974, *Electrodynamics of Plasmas*. Nauka, Moscow
- Aschwanden M.J., Benz A.O., 1988, *ApJ* 332, 447
- Aschwanden M., 1990a, *A&A* 237, 512
- Aschwanden M.J., 1990b, *A&AS* 85, 1141
- Bastian T.S., Bookbinder J., Dulk G.A., Davis M., 1990, *ApJ* 353, 265
- Dory R.A., Guest G.E., Harris E.G., 1965, *Phys. Rev. Lett.* 14, 131
- Fleishman G.D., 1994a, *Solar Phys.* 153, 367
- Fleishman G.D., Yastrebov S.G., 1994b, *Solar Phys.* 153, 389
- Fleishman G.D., Yastrebov S.G., 1994c, *Solar Phys.* 154, 361
- Fleishman G.D., Melnikov V.F., 1998, *Uspekhi Fiz. Nauk* V. 168, 1265 (engl. translation: *Physics-Uspekhi* 41, 1157)
- Fleishman G.D., Korsakov V.B., 1999, *Proc. of 9. European Meeting on Solar Physics, Magnetic Fields and Solar Processes, Firenze, Italy, Sept. 12–18, 1999*
- Fu Q.J., Huang G.L., 1998, *Proc. CESRA 98 workshop, Univ. Helsinki*, 16
- Galopeau P., Zarka P., Le Queau D., 1989, *J. Geophys. Res.* 94, 8793
- Güdel M., Benz A.O., 1990, *A&A* 231, 202
- Hamilton J.R., Lu E.T., Petrosian V., 1990, *ApJ* 354, 726
- Karlicky M., Sobotka M., Jiricka K., 1996, *Solar Phys.* 168, 375
- Korsakov V.B., Fleishman G.D., 1998, *Izv. vuzov-Radiofizika* 41, 46 (engl. transl.: *Radiophysics and Quantum Electronics*)
- Korsakov V.B., 1997, *Diploma work, State Technical University, St. Petersburg, Russia*
- Ledenev V.G., 1998, *Solar Phys.* 179, 405
- Li H.W., 1986, *Solar Phys.* 104, 131
- Melnikov V.F., Tikhomirov Yu.V., Snegizev S.D., Alexeev V.A., Lipatov B.N., 1999, *Izv. vuzov-Radiofizika*, in press
- Melnikov V.F., Magun A., 1998, *Solar Phys.* 178, 153
- Melrose D.B., Hewitt R.J., Dulk G.A., 1984, *J. Geophys. Res.* 89, 897
- Melrose D.B., 1980, *Plasma Astrophysics*. Gordon & Breach, New York
- Press W.H., Flannery B.P., Teukolsky S.A., Vetterling W.T., 1998, *Numerical Recipes in C*. Cambridge Univ. Press
- Pritchett P.L., 1986, *Phys. Fluids* 29, 2919
- Sharma R.R., Vlahos L., 1984, *ApJ* 280, 405
- Ladreitner H.P., Leblanc Y.J., 1990, *Geophys. Res.* 95, 6423

- Slotje C., 1981, Atlas of fine structures at dynamical spectra of solar type IV - dm and some type II radio bursts. Dwingeloo Observatory
- Stähli M., Magun A., 1986, Solar Phys. 104, 117
- Swanson D.G., 1989, Plasma Waves. Academic Press, New York
- Winglee R.R., Dulk G.A., 1986, Solar Phys. 104, 93
- Winglee R.R., Dulk G.A., Pritchett P.L., 1988, ApJ 328, 809
- Winglee R.M., Menietti J.D., Wong H.K.J., 1992, Geophys. Res. 97, 17131
- Wu C.S., Tsai S.T., Xu M.J., Shen J.W., 1981, ApJ 248, 384
- Wu C.S., 1985, Space Sci. Rev. 41, 215